

3FGL DEMOGRAPHICS OUTSIDE THE GALACTIC PLANE USING SUPERVISED MACHINE LEARNING: PULSAR AND DARK MATTER SUBHALO INTERPRETATIONS

N. MIRABAL,^{1,2} E. CHARLES,³ E. C. FERRARA,¹ P. L. GONTHIER,⁴ A. K. HARDING,¹ M. A. SÁNCHEZ-CONDE,^{5,6} & D. J. THOMPSON¹

¹ NASA Goddard Space Flight Center, Greenbelt, MD 20771, USA

² NASA Postdoctoral Program Fellow, USA

³ W. W. Hansen Experimental Physics Laboratory, Kavli Institute for Particle Astrophysics and Cosmology, Department of Physics and SLAC National Accelerator Laboratory, Stanford University, Stanford, CA 94305, USA

⁴ Hope College, Department of Physics, Holland, MI 49423 USA

⁵Department of Physics, Stockholm University, AlbaNova, SE-106 91 Stockholm, Sweden

⁶The Oskar Klein Centre for Cosmoparticle Physics, AlbaNova, SE-106 91 Stockholm, Sweden

Draft version May 4, 2016

ABSTRACT

Nearly 1/3 of the sources listed in the Third *Fermi* Large Area Telescope (LAT) catalog (3FGL) remain unassociated. It is possible that predicted and even unanticipated gamma-ray source classes are present in these data waiting to be discovered. Taking advantage of the excellent spectral capabilities achieved by the *Fermi* LAT, we use machine learning classifiers (Random Forest and XGBoost) to pinpoint potentially novel source classes in the unassociated 3FGL sample outside the Galactic plane. Here we report a total of 34 high-confidence Galactic candidates at $|b| \geq 5^\circ$. The currently favored standard astrophysical interpretations for these objects are pulsars or low-luminosity globular clusters hosting millisecond pulsars (MSPs). Yet, these objects could also be interpreted as dark matter annihilation taking place in ultra-faint dwarf galaxies or dark matter subhalos. Unfortunately, *Fermi* LAT spectra are not sufficient to break degeneracies between the different scenarios. Careful visual inspection of archival optical images reveals no obvious evidence for low-luminosity globular clusters or ultra-faint dwarf galaxies inside the 95% error ellipses. If these are pulsars, this would bring the total number of MSPs at $|b| \geq 5^\circ$ to 106, down to an energy flux $\approx 4.0 \times 10^{-12}$ erg cm⁻² s⁻¹ between 100 MeV and 100 GeV. We find this number to be in excellent agreement with predictions from a new population synthesis of MSPs that predicts 100–126 high-latitude 3FGL MSPs depending on the choice of high-energy emission model. If, however, these are dark matter substructures, we can place upper limits on the number of Galactic subhalos surviving today and on dark matter annihilation cross sections. These limits are beginning to approach the canonical thermal relic cross section for dark matter particle masses below ~ 100 GeV in the bottom quark ($b\bar{b}$) annihilation channel.

Subject headings: dark matter – gamma rays: general – pulsars: general

1. INTRODUCTION

There is compelling evidence for the existence of dark matter in the Universe. Already in 1933, Zwicky (1933) had collected enough data to postulate the presence of more mass than what could be inferred from visible galaxies. Over the past 80 years, additional observations ranging from the rotation curves of spiral galaxies (Rubin, Thonnard, & Ford 1978) to large-scale structure (Ade et al. 2014; Betoule et al. 2014) seem to point in the same direction. One outstanding prediction of cosmological simulations using cold dark matter particles is that the Milky Way halo should be heavily populated with thousands of smaller dark matter subhalos as a result of the hierarchical assembly process (Klypin et al. 1999; Moore et al. 1999; Springel et al. 2008). Dark matter subhalos would include any dark matter configuration, from those hosting the largest known dwarf spheroidal galaxies in the Milky Way to the lightest predicted dark matter substructures with masses around $10^{-4}M_\odot$ (Ricotti & Gould 2009; Scott & Silvertsson 2010). Conceptually in this scenario, the bulk of the subhalo population is made up by small-scale dark matter substructures with limited or null star formation, which would be almost impossible to detect in existing optical surveys.

Should dark matter subhalos without major star for-

mation episodes exist in large numbers, one of the only ways to detect them might be by tracking gamma rays from dark matter annihilation. The all-sky coverage and unprecedented sensitivity of the Large Area Telescope (LAT), on board NASA’s *Fermi* satellite, is enabling the most effective search for potential dark matter subhalos to date. The obvious place to look for subhalo candidates is among the 3033 sources detected and characterized in the Third *Fermi*–LAT catalog (3FGL) (Acero et al. 2015), in particular, among the 1010 sources listed as unassociated with counterparts of known gamma-ray-producing source classes. It is plausible that after years of observations, *Fermi* has already detected dark matter subhalos. The challenge now is to locate them (Charles et al. 2016).

Previous attempts to pinpoint dark matter subhalos have systematically searched for unassociated sources with spectra that are consistent with dark matter annihilation (Buckley & Hooper 2010; Nieto et al. 2011; Belikov, Hooper & Buckley 2012; Zechlin & Horns 2012; Ackermann et al. 2012a; Berlin & Hooper 2014; Bertoni, Hooper, & Linden 2015, 2016). Machine-learning classification targeting dark matter subhalos has also been performed using k -means clustering in the First *Fermi* LAT Catalog (1FGL) (Mirabal et al. 2010)

and Random Forest in the Second *Fermi* LAT Catalog (2FGL) (Mirabal et al. 2012). Here we present an application of machine-learning classifiers that aims to chart all Galactic sources outside the plane in the 3FGL. By specifically isolating 3FGL objects at high latitude we hope to reduce the search space for dark matter subhalos and unknown source classes as much as possible. The paper is organized as follows. In Section 2 we introduce the spectral prescription for locating Galactic objects outside the plane in the 3FGL. In Section 3 we introduce machine-learning classifiers. Section 4 covers training sample and variable selection. In Sections 5 and 6 we discuss cross validation and prediction results. In Section 7, we discuss possible interpretations of the results including a visual search for ultra-faint dwarf galaxy and globular cluster counterparts, as well as direct comparison with statistics from pulsar population synthesis models. We also place constraints on the annihilation cross section by comparing the number of potential subhalos to predictions from cosmological simulations. Finally, in Section 8 we present our conclusions and outlook.

2. SPECTRAL PRESCRIPTION FOR THE GALACTIC POPULATION OUTSIDE THE PLANE

At high Galactic latitude, the totality of known Galactic gamma-ray emitters correspond to pulsars or globular clusters hosting MSPs (Acero et al. 2015). Two additional undiscovered gamma-ray-producing source classes have been postulated to exist: dark matter subhalos (Bergström et al. 1999) and dwarf galaxies (Lake 1990). Dark matter annihilation is expected to dominate the gamma-ray signal from both known Galactic dwarf galaxies and from dark matter subhalos. If two dark matter particles annihilate through typical Standard Model channels, the decay and hadronization of these particles would create a gamma-ray spectrum that extends up to the rest mass of the dark matter particle with a sharp cutoff (Bergström, Ulio, & Buckley 1998; Fornengo, Pieri & Scopel 2004). The gamma-ray spectrum is given by

$$\frac{d\Phi}{dE}(E, \Delta\Omega) = \frac{1}{4\pi} \frac{\langle\sigma v\rangle}{2m_\chi^2} \frac{dN_\gamma}{dE} \times J(\Delta\Omega), \quad (1)$$

where $\langle\sigma v\rangle$ is the thermally averaged annihilation cross section, m_χ is the dark matter particle mass, and $\frac{dN_\gamma}{dE}$ is the gamma-ray yield per annihilation and depends on the particle physics model under consideration (Sjostrand, Mrenna & Skands 2006).

The second part of the equation, or the so-called astrophysical factor $J(\Delta\Omega)$, corresponds to the integration of the dark matter density squared $\rho^2(l, \Omega)$ along the line of sight l over a solid angle $\Delta\Omega$. The nearest and/or most massive dark matter subhalos would be easiest to detect even if they host no stars.

Figure 1 shows the predicted gamma-ray spectrum for the annihilation of 30 GeV dark matter particles into bottom quark ($b\bar{b}$) pairs. The spectral shape from dark matter annihilation would be quite recognizable. Unfortunately, a dark matter annihilation spectrum around a few GeV would not be unique. Most known gamma-ray pulsars display nearly identical spectra with sharp exponential cutoffs (Baltz, Taylor & Wai 2007; Abdo et al. 2013). To illustrate this point, we have overlaid in Fig-

ure 1 a typical MSP spectrum drawn from the Second *Fermi* LAT Pulsar Catalog (2FPC) (Abdo et al. 2013).

This pulsar-dark matter spectral degeneracy has driven a lively debate about the origin of excess GeV emission at the Galactic center (Goodenough & Hooper 2009; Hooper & Linden 2011; Abazajian & Kaplinghat 2012; Mirabal 2013; Gordon & Macias 2013; Yuan & Zhang 2014; Daylan et al. 2014; Carlson & Profumo 2014; Petrović, Serpico & Zaharijas 2015; Calore, Cholis & Weniger 2015; Brandt & Kocsis 2015; Bartels, Krishnamurthy, & Weniger 2016; Lee et al. 2016; Ajello et al. 2016; O’Leary et al. 2016); however, the spectral degeneracy permeates to other astrophysical settings beyond the Galactic center. Indeed, because of this gamma-ray degeneracy, one cannot expect to distinguish spectrally between pulsars, low-luminosity globular clusters hosting MSPs, ultra-faint dwarf galaxies, and dark matter subhalos.

By contrast, none of the known extragalactic sources have exponentially curved LAT spectra, except for the Large Magellanic Cloud (LMC) pulsar (Ackermann et al. 2015b). Variability is also a far more likely characteristic of extragalactic objects than of Galactic objects at high latitude. One can turn the spectral degeneracy between some Galactic classes and the marked contrast with extragalactic objects into assets by using known pulsar and globular cluster gamma-ray spectra to help hunt down undiscovered dark matter subhalos and ultra-faint dwarf galaxies in the 3FGL with machine-learning classifiers. We describe such search strategy next.

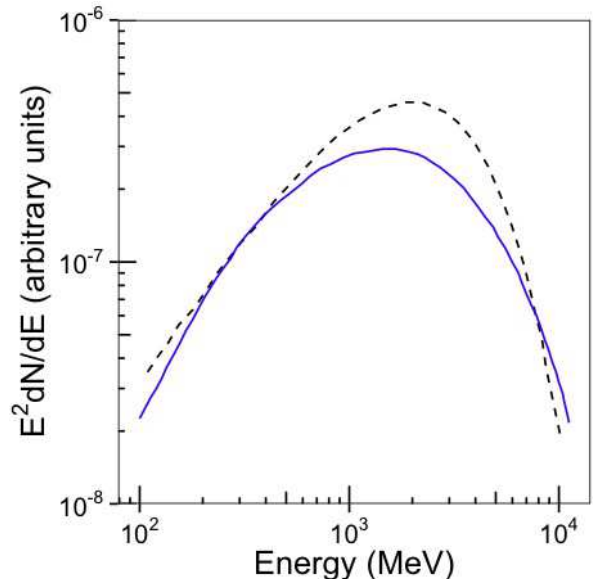


FIG. 1.— Spectral shape from dark matter annihilation (blue line) of a 30 GeV particle into bottom quark ($b\bar{b}$) pairs (Fornengo, Pieri & Scopel 2004). Other Standard Model annihilation channels are expected to produce similar spectra. Also shown is a representative MSP spectrum (black dashed line) from the 2FPC (Abdo et al. 2013).

3. MACHINE-LEARNING CLASSIFIERS

By machine learning classifier, we denote any algorithm with the ability to perform accurate predictions, after having trained on the properties of a well-known

training set of data. For most of this work, we will concentrate on supervised machine learning classifiers or sets of models that can input a list of variables of a data set and output a prediction model that best describes the relationship between the variables and known classes. For an overview of popular machine-learning classifiers, we refer the reader to Hastie, Tibshirani, & Friedman (2001). Among the plethora of available machine-learning classifiers, we have settled on two highly accurate variants of classification trees, i.e. Random Forest and XGBoost (Fernandez-Delgado et al. 2014; Chen & Guestrin 2016).

3.1. *Random Forest*

Random Forest is an ensemble learning method that grows a large forest of randomized classification trees and aggregates their predictions made from a list of input variables (Breiman 2001). Individual classification trees are constructed by randomly sampling k variables from n input variables at each node (Quinlan et al. 1994). The forest selects a random sample with replacement from the original training set using bagging (bootstrap aggregating). Any data left out of the bootstrap sample helps to measure the internal accuracy directly in the form of an out-of-bag estimates. To classify an object, each tree in the forest issues a prediction. The predictions from all trees for the same object are then collected and a class is determined through a majority decision. Aside from being easy to use, Random Forest provides outstanding performance and the ability to track proximity matrices. We adopted the *randomForest* set of routines, which implements the original Random Forest for classification and regression to the R language (Liaw & Wiener 2002). The final model is based on 1000 trees, with a total of \sqrt{p} variables sampled at each split, where p is the final number of variables.

3.2. *XGBoost*

The eXtreme Gradient Boosting XGBoost¹ is a modified version of gradient boosting (Friedman 2001). The fundamental difference with Random Forest is that XGBoost uses boosting to reweigh the training set sequentially (Quinlan et al. 1994). In contrast to bagging, boosting uses all instances at each repetition but issues a weight for each instance in the training set. These evolving weights adjust the learners to focus on different instances at each pass. One of the key problems in tree classifiers is how to find the best split at each node. To expedite this decision, XGBoost finds the best solution over all the possible splits according to percentiles of variable distribution (Chen & Guestrin 2016). In all experiments, we boost trees with a learning rate $\eta = 0.5$ and a maximum number of iterations set to 5.

4. TRAINING SAMPLE AND VARIABLE SELECTION

In order to construct a base training set for the Galactic population outside the plane, we use 143 3FGL pulsars identified by pulsations (PSRs), 15 3FGL globular clusters (glcs), and 24 3FGL pulsars with no pulsation seen in LAT yet (psrs). The extragalactic set includes 1745 sources from all AGN classes in the 3FGL.

It contains 3 non-blazar active galaxies (agn), 573 blazar candidates of uncertain type (BCU,bcu), 660 BL Lacs (BLL,bll), 484 flat-spectrum radio quasars (FSRQ,fsrq), 5 narrow-line Seyferts 1 (NLSY1,nlsy1), 15 radio galaxies (RDG,rdg), 3 soft spectrum radio quasars (ssrq), 1 compact steep spectrum quasar (css), and 1 Seyfert galaxy (sey). The entire dataset is divided into a training set (a random sample of 2/3 of the total) and a testing set (remaining 1/3 of the total).

Variable selection is essential to machine-learning classifiers. Starting from a set of parameters or variables the algorithm must be able to classify an object into one of a set of distinct classes. For any classification problem, there are certain variables that best capture a specific class of objects. The advantage of using machine-learning classifiers is that the algorithms can explore the entire variable space at once. Initially we started with a total of 35 3FGL variables, excluding positional, uncertainty and descriptive variables. In view of the inherent difficulties in sampling gamma-ray spectra for any given object, we augmented this original variable set with eight additional derived variables defined by hardness ratios $HR_{ij} = \frac{Flux_i - Flux_j}{Flux_i + Flux_j}$ and flux ratios $FR_{ij} = Flux_i / Flux_j$ between consecutive i, j bands for 0.1–0.3 GeV (Band 1), 0.3–1 GeV (Band 2), 1–3 GeV (Band 3), 3–10 GeV (Band 4), and 10–100 GeV (Band 5).

Figure 2 shows the out-of-bag error as a function of the number of variables used. The out-of-bag estimates tend to asymptote to a minimum at $n \gtrsim 8$. The value shown for $n = 2$ corresponds to the optimal scenario when using only `Signif_Curve` and `Variability_Index` as variables. For each classifier, we also quantify feature importance to pinpoint the features that best discriminate between classes. Table 1 ranks variable importance (from most to least important) in terms of the improvement achieved from each variable or *Gain* for all splits and trees for the XGboost model. For comparison, Table 2 ranks the overall percentage decrease in accuracy rate averaged over all trees or *MeanDecreaseAccuracy* measured by Random Forest (Liaw & Wiener 2002). As can be seen, the variable rankings are not identical but there is commonality on the top variables. The differences are an indication of the distinct paths the classifiers follow to achieve a successful prediction. After exploring different variable combinations, we find that the variables that most clearly differentiate Galactic and extragalactic populations include `Signif_Curve`, `Variability_Index`, and `Spectral_Index`. We also include flux ratios and hardness ratios for five energy bands in our final models.

5. CROSS VALIDATION

During initial tests, we quickly found out that Random Forest suffered from the fact that the training set was highly imbalanced, i.e. 90% extragalactic versus 10% Galactic trainees. As constructed, Random Forest tends to build classification trees dominated by the majority class. To alleviate this problem, we artificially increased the training set using over-sampling as implemented in the Synthetic Minority Over-sampling Technique (*SMOTE*) (Chawla et al. 2002). *SMOTE* creates a much larger synthetic minority class by replicating the existing sample using five nearest neighbors. With the *SMOTE* approach we were able to achieve a test

¹ <https://github.com/dmlc/xgboost>

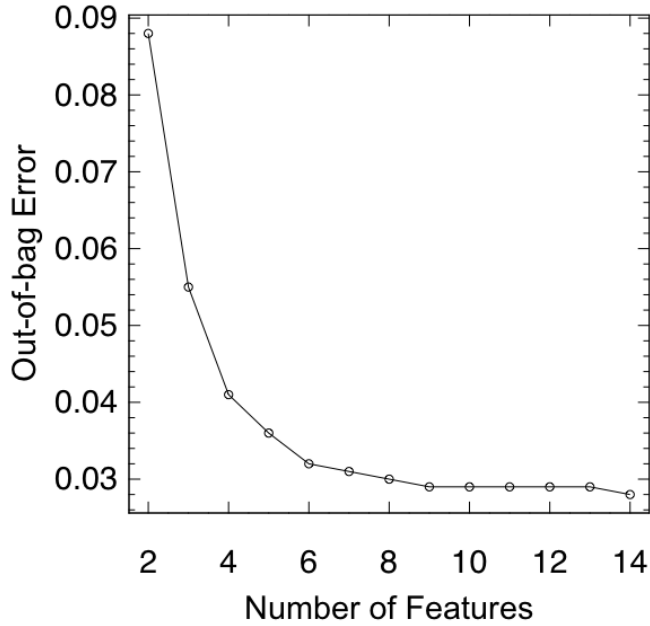


FIG. 2.— Out-of-bag estimates as a function of the number of variables used by the classifier.

TABLE 1
3FGL VARIABLE
IMPORTANCE ACCORDING TO
Gain IN XGBOOST.

Variable	<i>Gain</i>
Signif_Curve	0.47
Variability_Index	0.26
FR ₄₅	0.10
Spectral_Index	0.08
FR ₁₂	0.03
FR ₂₃	0.03
Pivot_Energy	0.02
FR ₃₄	0.01

TABLE 2
3FGL VARIABLE IMPORTANCE ACCORDING TO
MeanDecreaseAccuracy IN RANDOM FOREST.

Variable	<i>MeanDecreaseAccuracy</i>
Variability_Index	0.58
FR ₄₅	0.40
Signif_Curve	0.40
Pivot_Energy	0.33
HR ₄₅	0.30
Spectral_Index	0.26
HR ₂₃	0.24
FR ₂₃	0.22

set error rate of 2.8% for Random Forest. Class imbalanced was not a problem for XGBoost and the training was done with the original training and testing samples, reaching a test set error rate of 3.3%.

Figure 3 shows the receiver operating characteristic (ROC) curves for both classifiers (Hastie, Tibshirani, & Friedman 2001). At various threshold values, we plot the true positive rate (the fraction of correctly identi-

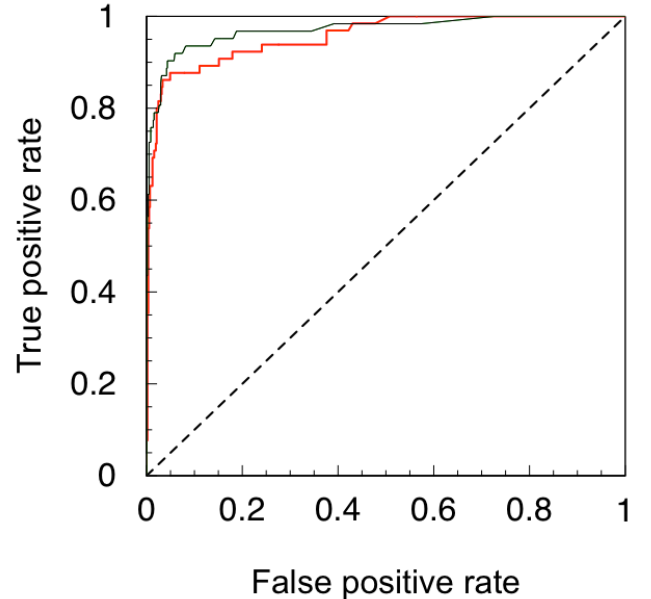


FIG. 3.— The Receiver Operating Characteristic (ROC) curves for Random Forest (black line) and XGBoost (red line). The closer the curve to the upper left corner, the better the performance. The 45° dashed line marks the region where true positive and false positive rates are equal.

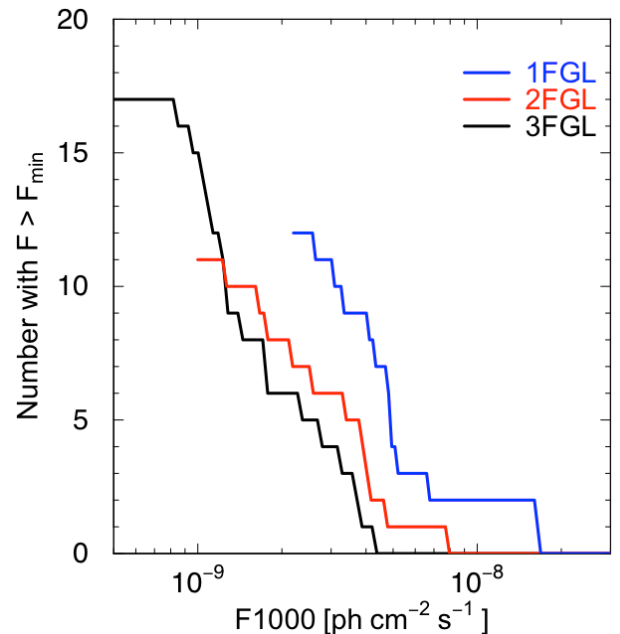


FIG. 4.— Number of potential 3FGL Galactic candidates at $|b| \geq 20^\circ$ (black). Also shown are 1FGL (blue) and 2FGL (red) candidates using the same machine-learning approach. F1000 represents the photon flux for the 1–100 GeV energy range.

fied) versus the false positive rate (the fraction of candidates incorrectly classified). As shown, Random Forest slightly outperforms XGBoost, but only after taking into account the class imbalance. A perfect classifier would have a true positive rate equal to one.

A complementary measure of accuracy can be accomplished by applying Random Forest and XGBoost retroactively to unassociated sources listed in the 1FGL and 2FGL. Since a number of *Fermi* discoveries have been

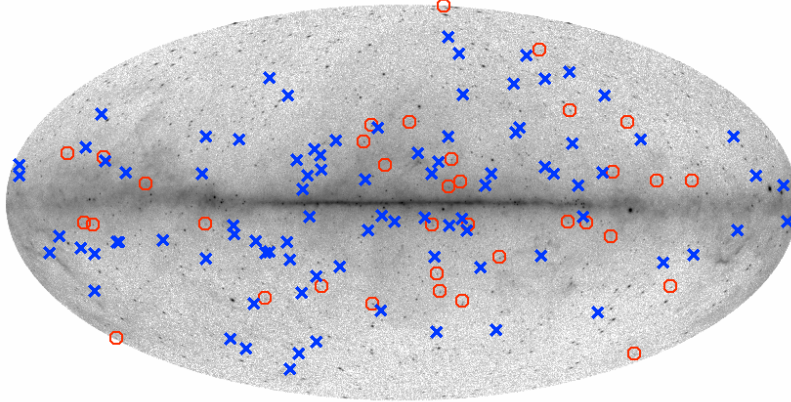


FIG. 5.— Galactic distribution of 34 high-latitude Galactic candidates (red circles) superimposed on a smoothed *Fermi* LAT all-sky map for energies $E \geq 1$ GeV based on events collected during the period 2008 August 4–2015 August 4 (Credit: *Fermi* LAT Collaboration). High-latitude 3FGL pulsars (blue crosses) are also plotted for comparison.

made since those early catalogs were first released, we can now directly measure how many high-latitude Galactic candidates selected using machine-learning classifiers have been confirmed either as pulsars or globular clusters. Out of 22 Galactic candidates above 10σ significance picked by the classifiers in the 1FGL, 18 have been confirmed as pulsars to date. This implies that the accuracy achieved by the classifiers exceeds 80% at that significance level. In Figure 4 we show the number of 3FGL Galactic candidates at $|b| \geq 20^\circ$ as a function of flux. For comparison, 1FGL and 2FGL candidates using the same machine-learning classifiers are also shown. We can clearly see the tremendous progress in pulsar discoveries since the release of the 1FGL based on 11 months of *Fermi* LAT data.

6. PREDICTION RESULTS

Next we applied the classifier models to the entire 3FGL unassociated sample. In order to focus on sources outside the Galactic plane, we excluded unassociated 3FGL sources within 5° of the plane. This cut leaves us with a starting list of 675 unassociated objects from a total of 1010. Since we are only interested in high-quality predictions, we further impose the condition that in order to retain a Galactic candidate both classifiers must agree (probability $P_{\text{Galactic}} \geq 0.5$ that the object is Galactic in both classifiers). Finally, we only report predictions for 3FGL objects with a detection significance $\geq 10\sigma$.

Based on these criteria, we find a total of 34 high-latitude Galactic candidates with energy flux $\gtrsim 4.0 \times 10^{-12}$ erg cm $^{-2}$ s $^{-1}$ between 100 MeV and 100 GeV at $|b| \geq 5^\circ$. Table 3 lists these candidates. To check for consistency, we compared our list of candidates with results from spectral fitting of 3FGL unassociated sources (Bertoni, Hooper, & Linden 2015), as well as with pulsar predictions using a combination of Random Forest and Logistic Regression (Saz Parkinson et al. 2016). The list of Galactic candidates at high Galactic latitude is in good

agreement with both of these works.

7. INTERPRETATIONS

Armed with these 34 potential high-latitude Galactic objects, we can now place the results in context of known and hypothesized gamma-ray source classes.

7.1. Globular Clusters/Dwarf Galaxies: Optical Search

One possibility is that some of these newly discovered objects are either low-luminosity globular clusters (Koposov et al. 2007; Minniti et al. 2011) or ultra-faint dwarf galaxies. In order to examine this possibility we have visually inspected Digitized Sky Survey (DSS) and Sloan Digital Sky Survey (SDSS) images (Ahn et al. 2014). We confined our visual inspection to the area enclosed within the 3FGL 95% uncertainty ellipses of the 34 candidates. Our search mainly focused on visually diffuse and extended objects in the optical, but none were found at least 1 magnitude above the DSS optical limit. It is important to note that the visual approach is limited to objects that can easily stand out in the images but it is severely hampered when trying to reach ultra-faint dwarf galaxies as the ones detected by SDSS (Willman et al. 2005) and DES (Bechtol et al. 2015).

For six optical fields with reliable multi-band SDSS photometry (3FGL J0318.1+0252, 3FGL J1120.6+0713, 3FGL J1225.9+2953, 3FGL J1625.1-0021, 3FGL J2103.7-1113, 3FGL J2212.5+0703), we systematically searched for unusual concentrations of RR Lyrae. RR Lyrae stars are excellent distance indicators, as well as superb tracers of stellar substructures away from the Galactic plane (Mateo et al. 1996; Alcock et al. 1997). In order to pinpoint RR Lyrae star candidates within the 3FGL 95% uncertainty ellipses, we adopted a simple SDSS color cut scheme based on Equations 1–4 derived by Sesar, Ivezić, & Grammer (2010).

We find no anomalous excess of RR Lyrae stars in any of the 6 fields with significance greater than 5σ . It is quite possible that fainter stellar structures with very few members could be present below the optical detection limits (Willman et al. 2005; Bechtol et al. 2015).

7.2. Pulsars: Comparison with Population Synthesis Models

Given the ultra-fast pace of pulsar discoveries with *Fermi*, it is not surprising that at least five of the Galactic candidates identified here have been already confirmed as pulsars since the 3FGL release (see Table 3). In the 3FGL there are 89 pulsars listed at $|b| \geq 5^\circ$ with energy flux larger than $\gtrsim 2.3 \times 10^{-12} \text{ erg cm}^{-2} \text{ s}^{-1}$ between 100 MeV and 100 GeV. Of the 89 known high-latitude gamma-ray pulsars, 77 are MSPs with spin period P (s) and spin-down rate \dot{P} satisfying $\log_{10} \dot{P} + 19.5 + 2.5 \log_{10} P < 0$ (Acero et al. 2015). An addition of 34 pulsars would bring the total number of *Fermi* LAT detected pulsars at high latitude to 123.

In order to compare this number to theoretical predictions from pulsar simulations, we performed a new population synthesis of MSPs (Gonthier 2016; Gonthier et al. 2016a,b) in a similar fashion as in the study of Story, Gonthier, & Harding (2007). However, we have used improved pulsar spin-down formalism, empirical gamma-ray luminosity, and beam geometries of the high-energy emission models of the high-altitude Slot Gap (two pole caustic) (Muslimov & Harding 2003, 2004) (TPC), of the Outer Gap (Cheng, Ho, & Ruderman 2000; Cheng, Ruderman, & Zhang 2000; Zhang, Fang, & Chen 2007) (OG), and of the pair-starved polar cap (Muslimov & Harding 2004, 2009) (PSPC).

In addition to the radio beam geometry used in Story, Gonthier, & Harding (2007), we implemented a radio aligned model (ALTPC) in which the radio emission has the same geometry as the high-energy TPC model. The characteristics of thirteen radio surveys provided the detection thresholds for simulated radio pulsars, and the *Fermi* point source threshold map in the 2FPC was scaled for various observing periods to determine the detection of simulated gamma-ray pulsars.

The models predict that *Fermi* LAT should detect anywhere from 100 to 126 MSPs in four years with an energy flux larger than $2.3 \times 10^{-12} \text{ erg cm}^{-2} \text{ s}^{-1}$ at $|b| \geq 5^\circ$ (Table 4). Assuming that 85% of the 34 Galactic candidates are MSPs, as is observed in the 3FGL catalog at high Galactic latitude, then the total number of 3FGL MSPs at $|b| \geq 5^\circ$ would be ≈ 106 (see Table 4). Therefore, the simulated pulsar population is in excellent agreement with the projected number of 3FGL MSP detections. In fact, depending on the pulsar emission model there is some wiggle room (≈ 4 – 20) for additional 3FGL MSP discoveries at high Galactic latitude. Below 10σ and above 4σ significance, the machine-learning classifiers find an additional 33 Galactic candidates that could easily cover this difference. The locations of the 34 high-significance Galactic candidates and known 3FGL pulsars at $|b| \geq 5^\circ$ are shown in Figure 5.

7.3. Dark Matter Subhalos: Comparison with Aquarius and Via Lactea II Numerical Simulations

Taking advantage of the predictions in Bertoni, Hooper, & Linden (2015), we can also directly compare the number of Galactic candidates at $|b| \geq 20^\circ$ to the expected number of nearby subhalos detectable by *Fermi* LAT after four years of observations. Because our classifiers rely on the 3FGL variables, we are only sensitive to dark matter annihilation in the 100 MeV–300 GeV energy range. It is important to note that no significantly exponentially curved candidates at energies $\gtrsim 300$ GeV have been found in any of the hard *Fermi*-LAT source catalogs (Ackermann et al. 2016). As in the original approach outlined in Berlin & Hooper (2014), the subhalo predictions in Bertoni, Hooper, & Linden (2015) rely on the distribution of hundreds of thousands of subhalos that were simulated in 6 ultra-highly resolved Milky-Way sized halos as part of the Aquarius Project (Springel et al. 2008).

Bertoni, Hooper, & Linden (2015) calculated the number of detectable Aquarius subhalos as a function of *Fermi* LAT flux and Galactic latitude. Recently, Schoonenberg et al. (2016) used results of the Via Lactea II simulation (Diemand, Kuhlen, & Madau 2007) scaled to the Planck 2015 cosmological parameters and found a slightly smaller number of detectable subhalos, but still consistent with the Aquarius results considering the range of assumptions involved. For our comparison of high-latitude candidates with dark matter predictions, we removed recently detected pulsars from Table 3. This brings down the number of $|b| \geq 20^\circ$ subhalo candidates from 17 to 14.

Figure 6 shows the upper limits on $\langle\sigma v\rangle$ for dark matter masses m_χ between 30 GeV and 10 TeV annihilating into a bottom quark ($b\bar{b}$) final states based on the detection of 14 potential subhalo candidates at $|b| \geq 20^\circ$. Note that these limits would only be slightly better if one includes the role of halo substructure to boost the subhalo annihilation flux (Sánchez-Conde & Prada 2014; Moliné et al. 2016). More precisely, following Moliné et al. (2016), we estimate at most a factor $\sim 10\%$ stronger limits when boosting the annihilation signal in the mass range 10^4 – $10^7 M_\odot$. For comparison, we also show constraints if eventually no dark matter subhalos turn up in the 3FGL from the Aquarius (Bertoni, Hooper, & Linden 2015) and Via Lactea II simulations (Schoonenberg et al. 2016) respectively. While the current limit is not constraining enough to rule out the canonical thermal relic cross section at energies below 100 GeV (Steigman, Dasgupta, & Beacom 2012), the curve is starting to approach competitive values. Indeed, further associations of some of these candidates with conventional astrophysical sources may only lead to more stringent limits.

As noted by Bertoni, Hooper, & Linden (2015), there are significant uncertainties in the number of predicted dark matter subhalos that could shift these dark matter limits by a factor of a few. The point remains that *Fermi* LAT might have detected several dark matter subhalos by now, even under the most pessimistic assumptions. The absence of an overwhelming number of subhalo candidates provides complementary verification of more robust annihilating dark matter limits inferred from dwarf galaxies (Geringer-Sameth, Koushiappas, & Walker 2015; Ackermann et al. 2015a) and the Galactic center (Abazajian & Kaplinghat 2012; Gordon & Macias

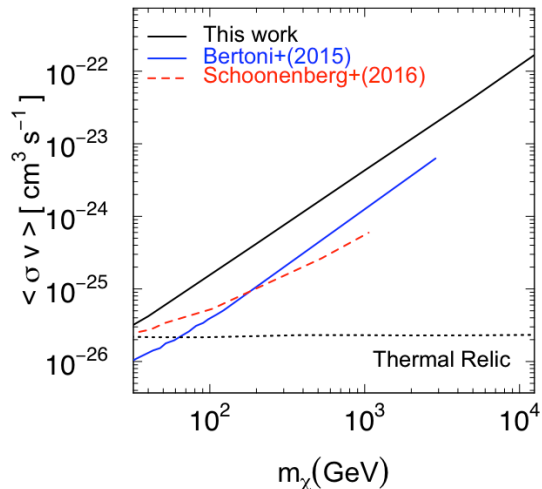


FIG. 6.— Upper limits on the dark matter annihilation cross section for the bb channel assuming 14 subhalo candidates at $|b| \geq 20^\circ$ (black solid line). The dashed red line is an upper limit derived from the Via Lactea II simulation when zero 3FGL subhalos are adopted (Schoonenberg et al. 2016). The blue line corresponds to the constraint for zero 3FGL subhalo candidates using the Aquarius simulation instead (Bertoni, Hooper, & Linden 2015). The horizontal dotted line marks the canonical thermal relic cross section (Steigman, Dasgupta, & Beacom 2012).

2013; Calore, Cholis & Weniger 2015; Daylan et al. 2014).

8. CONCLUSIONS AND OUTLOOK

We find that the set of variables provided in the *Fermi* LAT catalogs have the ability to effectively predict gamma-ray source classes in the 3FGL dataset. After careful examination of various Galactic demographics, we find that the 34 additional high-latitude Galactic candidates predicted using machine-learning classifiers can be accommodated by existing pulsar population synthesis models without the need to introduce undiscovered globular clusters, dark matter subhalos, or gamma-ray emitting ultra-faint dwarf galaxies. On the other hand, if these objects were produced by annihilating dark matter, the upper limits on the annihilation cross section are starting to approach values at or below the canonical thermal cross section for energies $\lesssim 100$ GeV.

The discovery of radio and gamma-ray pulsations will be crucial to address the spectral degeneracy between dark matter annihilation and pulsar emission. However,

blind searches will face greater obstacles in noisy MSPs and fainter gamma-ray sources as *Fermi* continues operations. Table 4 shows projected discoveries of MSPs for 10 years of *Fermi* LAT data taking. The most promising follow-up strategy to break these degeneracies will rest on our ability to detect pulsations going from the brightest to the faintest Galactic candidates. Some of these searches for the most elusive gamma-ray pulsars are being conducted by the distributed volunteer computing sources, *Einstein@Home* (Pletsch et al. 2013). New discoveries will require even larger computing resources and new search strategies.

Optical, ultraviolet and X-ray searches for binary objects with temporal variability could also enhance the chances for finding millisecond pulsars (Romani & Shaw 2011; Bogdanov & Halpern 2015). Incidentally, the addition of new MSPs will also bring us closer to the detection of nanohertz gravitational waves based on pulsar-timing arrays (Taylor et al. 2016). Should additional high-latitude Galactic candidates be confirmed as pulsars, new swaths of annihilation cross sections will be disfavored by direct comparison with statistics from cosmological numerical simulations of Milky Way-like galaxies. Therefore, subhalo searches represent a powerful complementary method to existing probes of dark matter annihilation.

Clearly, there ought to be dedicated multiwavelength campaigns to map the error ellipses of high-latitude Galactic candidates for which no radio/gamma-ray pulsations are found. Finally, the improvements in position and photon flux afforded by Pass 8 analysis (Atwood et al. 2013) should further enhance machine-learning predictions in the future *Fermi* LAT Fourth Source Catalog (4FGL).

Acknowledgments. This research was supported by a senior appointment to the NASA Postdoctoral Program at the Goddard Space Flight Center, administered by Universities Space Research Association through a contract with NASA. MASC is a Wenner-Gren Fellow and acknowledges the support of the Wenner-Gren Foundations to develop his research. We thank Seth Digel for helpful suggestions.

REFERENCES

- Abazajian K. N., & Kaplinghat M. 2012, *Phys. Rev.*, D86, 083511
 Abdo, A. A., Ajello, M., Allafort, A., et al. 2013, *ApJS*, 208, 17
 Acero, F., Ackermann, M., Ajello, M., et al. 2015, *ApJS*, 218, 23
 Ackermann, M., Albert, A., Baldini, L., et al. 2012a, *ApJ*, 747, 121
 Ackermann, M., Ajello, M., Allafort, A., et al. 2012b, *ApJ*, 753, 83
 Ackermann, M., Albert, A., Anderson, B., et al. 2015a, *Phys. Rev. Lett.*, 115, 231301
 Ackermann, M., Albert, A., Baldini, L., et al. 2015b, *Science*, 350, 801
 Ackermann, M., Ajello, M., Atwood, W., et al. 2016, *ApJS*, 222, 5
 Ade, P. A. R., Aghanim, N., Armitage-Caplan, C., et al. 2014, *A&A*, 571, A16
 Ajello, M., Albert, A., Atwood, W. B., et al. 2016, *ApJ*, 819, 44
 Ahn, C. P., Alexandroff, R., Allende Prieto, C., et al. 2014, *ApJS*, 211, 17
 Alcock, C., Allsman, R. A., Alves, D. R., et al. 1997, *ApJ*, 474, 217
 Atwood, W. D., Albert, A., Baldini, L., et al. 2013, ArXiv e-prints, arXiv:1303.3514
 Baltz, E. A., Taylor J. E., & Wai, L. L. 2007, *ApJ*, 659, L125
 Bartels, R., Krishnamurthy, S., & Weniger, C. 2016, *Phys. Rev. Lett.* 116, 051102
 Bechtol, K., Drlica-Wagner, A., Balbinot, E., et al. 2015, *ApJ*, 807, 50
 Belikov A. V., Buckley M. R., & Hooper D. 2012, *Phys. Rev. D*, 86, 043504
 Bergstrom, L., Ulio, P., & Buckley, J. H. 1998, *Ast. Phys.*, 9, 137
 Bergstrom, L., Edsjö, J., Gondolo, P., & Ulio, P. 1999, *Phys. Rev. D*, 59, 043506
 Berlin, A., & Hooper, D. 2014, *Phys. Rev. D*89, 016014
 Bertoni B., Hooper D., Linden T. 2015, *JCAP*, 12, 035
 Bertoni B., Hooper D., Linden T. 2016, preprint (arXiv:1602.07303)
 Betoule, M., Kessler, R., Guy, J., et al. 2014, *A&A*, 568, A22
 Bogdanov S., & Halpern J. P. 2015, *ApJ*, 803, L27

- Brandt, T. D., & Kocsis B. 2015, *ApJ*, 812, 15
- Breiman L., 2001, *Machine Learning*, 45, 5
- Buckley M. R., & Hooper D. 2010, *Phys. Rev.*, D82, 063501
- Calore F., Cholis I., & Weniger C. 2015, *JCAP*, 1503, 038
- Camilo, F., Kerr, M., Ray, P. S., et al. 2015, *ApJ*, 810, 85
- Carlson, E., Profumo, S. 2014, *Phys. Rev. D*, 90, 023015
- Charles, E., et al. 2016, in preparation
- Chawla, N. V., Bowyer, K. W., Hall L. O., & Kegelmeyer W. P. 2012, *JAIR*, 16, 321
- Chen, T., & Guestrin, C. 2016, preprint(arXiv:1603.02754)
- Cheng, K. S., Ho, C. & Ruderman, M. 1986, *ApJ*, 300, 500; 522
- Cheng, K. S., Ruderman, M., & Zhang, L. 2000, *ApJ*, 537, 964
- Daylan, T., Finkbeiner, D. P., Hooper, D., Linden, T., Portillo, S. K. N., Rodd, N. L., & Slatyer, T. R. 2016, *Physics of the Dark Universe*, 12, 1
- Diemand, J., Kuhlen, M., & Madau, P. 2007, *ApJ*, 657, 262
- Fernandez-Delgado, M., Cernadas, E., Barro, S., & Amorim, D. 2014, *Journal of Machine Learning Research*, 15, 3133
- Fornengo, N., Pieri, L., & Scopel, S. 2004, *Phys. Rev. D*, 70, 103529
- Friedman, J. 2001, *Ann. Stat.* 29, 1189
- Geringer-Sameth, A., Koushiappas, S. M., & Walker, M. G. 2015, *Phys. Rev. D*, 91, 083535
- Gonthier, P. L. 2016, in the Proceedings of "Origin, evolution and observable effects of the magnetic field in neutron stars" Workshop, Alicante, Spain
- Gonthier, P. L., Kow, Y-M., Harding, A. K., & Ferrara, E. C. 2016a, AAS 15th HEAD meeting, 114.08
- Gonthier, P. L., et al. 2016b, in preparation
- Goodenough L., & Hooper D. 2009, preprint (arXiv:0910.2998)
- Gordon, C., & Macias, O. 2013, *Phys. Rev. D*, 88, 083521
- Hastie, T., Tibshirani, R., & Friedman, J. 2001, *The Elements of Statistical Learning*, Vol. 1, page 339, Springer, New York
- Hooper, D., & Linden, T., 2011, preprint (arXiv:1110.0006)
- Klypin, A., Kravtsov, A. V., Valenzuela, O., & Prada, F. 1999, *ApJ*, 522, 82
- Koposov, S., de Jong, J. T. A., Belokurov, V., et al. 2007, *ApJ*, 669, 337
- Kuhlen M., Madau, P., & Silk, J. 2009, *Science*, 325, 970
- Lake, G. 1990, *Nature*, 346, 39
- Lee, S. K., Lisanti, M., Safdi, B. R., Slatyer, T. R., & Xue, W. 2016, *Phys. Rev. Lett.* , 116, 051103
- Liaw, A., Wiener, M. 2002, *R News*, 2/3, 18
- Mateo, M, Mirabal, N., Udalski, A., Szymanski, M., Kalyzny, J., Kubiak, M., Krzemiński, W., & Stanek, K. S. 1993, *ApJ*, 458, L13
- Minniti, D., Hempel, M., Toledo, I., et al. 2011, *A&A*, 527, 81
- Mirabal, N., Nieto, D., Pardo, S. 2010, preprint(arXiv:1007.2644)
- Mirabal, N., Frias-Martinez, V., Hassan, T., Frias-Martinez, E. 2012, *MNRAS*, 424, L64
- Mirabal, N. 2013, *MNRAS*, 436, 2461
- Moliné, A., Sánchez-Conde, M. A., Palomares-Ruiz, S., & Prada F. 2014, *MNRAS*, submitted (arXiv:1603.04057)
- Moore B., Ghigna, S., Governato, F., Lake, G., Quinn, T., Stadel, J., & Tozzi, P. 1999, *ApJ*, 524, L19
- Muslimov, A. G., & Harding, A. K. 2003, *ApJ*, 588, 430
- Muslimov, A. G., & Harding, A. K. 2004, *ApJ*, 606, 1143
- Muslimov, A. G., & Harding, A. K. 2009, *ApJ*, 692, 140
- Nieto, D., Martinez, V., Mirabal, N., Barrio, J. A., Satalecka, K., Pardo, S., & Lozano, I. 2011, preprint(arXiv:1110.4744)
- O'Leary, R. M., Kistler, M.D, Kerr, M., & Dexter, J. 2016, *Phys. Rev. D*, submitted(arXiv:1601.05797)
- Petrović, J., Serpico, P. D., & Zaharijas, G. 2015, *JCAP*, 2, 23
- Pletsch, H. J., Guillemot, L., Allen, B., et al. 2013, *ApJ*, 779, L11
- Ray, P., et al. 2016, *ApJ* (in preparation)
- Ricotti, M., & Gould, A. 2009, *ApJ*, 707, 979
- Quinlan J. R., 1993, *C4.5: Programs for Machine Learning*. Morgan Kaufmann Publishers, San Francisco, CA
- Romani, R. W., & Shaw, M. S. 2011, *ApJ*, 742, L1
- Rubin, V. C., Thonnard, N., & Ford W. K. 1978, *ApJ*, 225, L107
- Sánchez-Conde, M. A., & Prada F. 2014, *MNRAS*, 442, 2271
- Saz Parkinson, P. M., Xu H., Yu, P. L. H., Salvetti, D., Marelli M., & Falcone A. D. 2016, *ApJ*, accepted(arXiv:1602.00385)
- Schoonenberg, D., Gaskins, J., Bertone, G., & Diemand, J. 2016, preprint(arXiv:1601.06781)
- Scott P., & Sivertsson S. 2009, *PRL*, 103, 211301
- Sesar, B., Ivezić, Z., & Grammer, S. H. 2010, *ApJ*, 708, 717
- Sjostrand, T., Mrenna, S., & Skands, P. Z., *JHEP*, 0605, 026
- Springel, V., Wang, J., Vogelsberger, M., et al. 2008, *MNRAS*, 391, 1685
- Steigman, G., Dasgupta, B., & Beacom, J. F. 2012, *Phys. Rev. D*, 86, 023506
- Story, S. A., Gonthier, P. L. & Harding, A. K. 2007, *ApJ*, 671, 713
- Taylor, S. R., Vallisneri, M., Ellis, J. A., Mingarelli, C. M. F., Lazio, T. J. W., & van Haasteren, R. 2016, *ApJ*, 819, L6
- Willman, B., Blanton, M. R., West, A. A., et al. 2005, *AJ*, 129, 2692
- Yuan, Q., & Zhang, B. 2014, *JHEAp*, 3, 1
- Zhang, L., Fang, J., & Chen, S. B. 2007, *ApJ*, 666, 1165
- Zechlin, H.-S., & Horns, D. 2012, *JCAP*, 1211, 050
- Zwicky, F. 1933, *Helvetica Physica Acta*, 6, 110

TABLE 3
MACHINE-LEARNING GALACTIC CANDIDATES AMONG 3FGL UNASSOCIATED SOURCES AT $|b| \geq 5^\circ$.

Source Name	l (degrees)	b (degrees)	$P_{\text{Galactic}}(\text{RF})$	$P_{\text{Galactic}}(\text{XGBoost})$	ID or Assoc.
3FGL J0212.1+5320	134.93	-7.65	1.00	1.00	
3FGL J0238.0+5237	138.85	-6.92	0.94	0.85	
3FGL J0312.1-0921	191.51	-52.36	0.95	0.94	
3FGL J0318.1+0252	178.45	-43.64	1.00	1.00	
3FGL J0336.1+7500	133.11	15.50	0.98	1.00	
3FGL J0523.3-2528	228.20	-29.83	0.89	1.00	
3FGL J0545.6+6019	152.4964	15.7493	0.67	0.89	
3FGL J0758.6-1451	233.9599	7.5619	0.90	0.83	
3FGL J0802.3-5610	269.9308	-13.1755	0.72	0.90	
3FGL J0838.8-2829	250.6050	7.8008	0.97	1.00	
3FGL J0933.9-6232	282.2351	-7.8937	1.00	1.00	
3FGL J0953.7-1510	251.9380	29.6055	0.96	0.98	
3FGL J0954.8-3948	269.8445	11.4575	0.61	0.52	
3FGL J1035.7-6720	290.3908	-7.8284	1.00	1.00	psr (Camilo et al. 2015)
3FGL J1119.9-2204	276.4696	36.0588	0.97	1.00	
3FGL J1120.6+0713	251.5322	60.6852	0.85	0.73	
3FGL J1225.9+2953	185.1521	83.7648	0.94	1.00	
3FGL J1539.2-3324	338.7592	17.5342	0.90	1.00	
3FGL J1544.6-1125	356.2111	32.9844	0.63	0.73	psr (Bogdanov & Halpern 2015)
3FGL J1557.0-4225	335.6413	8.3622	0.50	0.57	
3FGL J1624.2-4041	340.5718	6.1421	1.00	1.00	PSR (<i>Einstein@Home</i> ^a)
3FGL J1625.1-0021	13.8808	31.8378	1.00	1.00	
3FGL J1653.6-0158	16.6181	24.9246	0.98	1.00	
3FGL J1702.8-5656	332.3978	-9.2447	0.62	0.84	
3FGL J1744.1-7619	317.1046	-22.4711	0.99	1.00	psr (Camilo et al. 2015)
3FGL J1753.6-4447	347.0854	-9.4164	0.98	0.99	
3FGL J1946.4-5403	343.8883	-29.5630	1.00	0.99	PSR (Ray et al. 2016)
3FGL J2039.6-5618	341.2312	-37.1551	0.98	1.00	
3FGL J2103.7-1113	37.8579	-34.4231	0.93	0.87	
3FGL J2112.5-3044	14.8984	-42.4487	0.99	0.99	
3FGL J2117.6+3725	82.7982	-8.2737	0.81	0.90	
3FGL J2133.0-6433	328.7390	-41.2683	0.93	1.00	
3FGL J2212.5+0703	68.7429	-38.5650	0.92	0.99	
3FGL J2233.1+6542	109.3427	6.5614	0.74	0.95	

^a <http://www.einsteinathome.org/>

TABLE 4
SUMMARY OF POPULATION SYNTHESIS OF MSPs AT $|b| \geq 5^\circ$.

Catalog	Period	Detected MSPs + (Galactic Candidates) ^a	Simulated			
			TPC	OG	AITPC	PSPC
3FGL	4 years	77 + (29)	110	126	104	100
	5 years		122	138	117	110
	10 years		160	173	167	145

^a Number listed in parentheses corresponds to 85% of Galactic candidates, as in the observed percentage of MSPs in the 3FGL pulsar list at high Galactic latitude.